Nanoscale

Accepted Manuscript

This article can be cited before page numbers have been issued, to do this please use: O. A. Douglas-Gallardo, G. J. Soldano, M. M. Mariscal and C. G. Sanchez, *Nanoscale*, 2017, DOI: 10.1039/C7NR04904H.

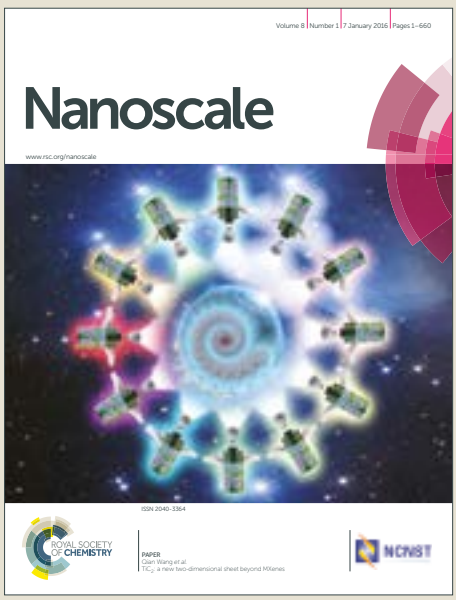

ROYAL SOCIETY OF CHEMISTRY

rsc.li/nanoscale

View Article Online
DOI: 10.1039/C7NR04904H

Journal Name

ARTICLE TYPE

Cite this: DOI: 10.1039/xxxxxxxxxx

Effects of Oxidation on the Plasmonic Properties of Aluminum Nanoclusters†

Oscar A. Douglas-Gallardo, Germán J. Soldano, Marcelo M. Mariscal and Cristián Gabriel Sánchez*

Received Date
Accepted Date

DOI: 10.1039/xxxxxxxxxx

www.rsc.org/journalname

The scouting of alternative plasmonic materials able to enhance and extend the optical properties of noble metal nanostructures is on the rise. Aluminum is endowed with a set of interesting properties that turn it into an attractive plasmonic material. Here we present the optical and electronic features of different aluminum nanostructures stemming from a multilevel computational study. Molecular Dynamics (MD) simulations using a reactive force field (ReaxFF), carefully validated with Density Functional Theory (DFT), were employed to mimic the oxidation of icosahedral aluminum nanoclusters. Resulting structures with different oxidation degrees were then studied through the Time-Dependent Density Functional Tight Binding (TD-DFTB) method. A similar approach was used on aluminum nanoclusters with a disordered structure to study how the loss of crystallinity affects the optical properties. To the best of our knowledge, this is the first report that addresses this issue from fully atomistic time-dependent approach by means of two different and powerful simulations tools able to describe quantum and physicochemical properties associated with nanostructured particles.

1 Introduction

The study of plasmonic properties of very small metallic particles have been mainly focused on gold and silver nanostructures [1–6]. Colloidal solutions of silver and gold nanostructures often exhibit an intense optical absorption band located on the visible region of the electromagnetic spectrum owing to coherent oscillations of conduction electrons in response to external electric fields [3,5]. These optical features along with their noble character render silver and gold nanostructures the ideal plasmonic metals. Nowadays, there is an extensive research of diverse materials that exhibit optical responses similar to noble metal nanostructures but with a plasmonic excitation located beyond the visible region. [7,8] In this context, aluminum appears as one of the most promising plasmonic materials. Not only it exhibits attractive plasmonic properties, but it is also biocompatible, abundant and a low-cost material. [9–12].

The plasmonic properties associated with very small aluminum nanostructures are characterized by having a single dipole surface plasmon resonance (SPR) band located below 400 nm within the ultraviolet region. [9–13]. Thereby, the plasmonic response of aluminum nanoclusters would fill up a region of the spectrum where the optical properties of silver and gold nanoclusters are intrinsically inactive. This distinctive optical feature would allow electronic coupling between plasmonic excitations and HOMO-LUMO transitions (220-280 nm) for a large number of bio- and organic molecules. [10,12]

From the synthetic point of view, the production of colloidal aluminum nanoclusters have been scarcely explored and only a few methods based on wet chemical have been proposed [13,14]. Despite its promising plasmonic properties, aluminum is well known for spontaneously form a thin oxide layer in presence of O_2. The oxide layer prevents the metal for further oxidation, a phenomenon known as passivation. Recently, a synthetic pathway for formation of bare aluminum nanoclusters in organic media has been reported [13]. In regular conditions, however, the formation of an oxide layer is inevitable. For nanostructured aluminum this oxidation process may modify its inherent plasmonic properties [11,12].

Theoretical studies of optical properties associated with different metallic nanostructures have been carried out through the use of several models and computational tools. Within the framework of methods based on classical electrodynamics, the discrete dipole approximation (DDA) has been one of the most widely used to explore and predict different optical phenomenon associated with particles with diverse compositions and morphologies [9–11,15–17].

INFIQC (UNC-CONICET), Departamento de Qumica Terica y Computacional, Facultad de Ciencias Qumicas, Universidad Nacional de Crdoba, Medina Allende y Haya de la Torre, Ciudad Universitaria, Crdoba, X5000HUA Crdoba, Argentina Fax: 54 351 5353850; Tel: 54 351 5353853; E-mail: cgsanchez@fcq.unc.edu.ar

† Electronic Supplementary Information (ESI) available: Validation of the Al-O ReaxFF from comparison with results obtained from DFT for small Al_xO_y clusters. See DOI: 10.1039/b000000x/

View Article Online
DOI: 10.1039/C7NR04904H

However, when the particle size is reduced (diameters of less than 10 nm) several size-related surface and quantum effects start to govern optical response and the DDA starts to loose validity. In this size domain, the optical response of metallic nanostructures can be obtained from methods based on time-dependent density functional theory (TD-DFT) approach. This approach includes all factors that determine the optical properties in a quantum regimen (depending on the nature of the exchange-correlationa functional used). Despite nowadays being the "weapon of choice" to study the absoprtion spectra of molecular systems, the method has a strong limitation with respect to the size of the approachable systems. This limitation is essentially related with computing cost. In recent years, many systems including silver[18–26], gold[21,22,27–34], aluminum[35,36] and bimetallic[32,37–40] nanostructures have been explored by using TD-DFT.

The optical properties of different aluminum nanostructures have been recently investigated using mainly the discrete dipole approximation (DDA) method.[9–11] Likewise, the effect of aluminum oxide over plasmonic properties have been studied using the same classical electrodynamics methods[10]. However, this type of approximation does not take into account the complex size-related-quantum effects that govern the optical properties for particles sizes below of 5 nm, nor the influence of the oxide layer on the electronic structure of the aluminum core. Despite the abundant research on the subject, the effect of oxygen on the optical properties of these nanostructures has not been undertaken from a fully atomistic approach. In order to do so, we have performed a multi-level systematic study combining Molecular Dynamics (MD), Density Functional Theory (DFT), and Quantum Dynamics. The optical absorption properties of bare icosahedral aluminum from 1.1 nm to 3.3 nm in diameter were explored and compared with those of the corresponding oxidized nanostructures.

2 Computational Method

2.1 Molecular Dynamics Simulations

Energy minimizations, molecular dynamics simulations, and simulated annealing were carried out using the Large-scale Atomic-Molecular Massively Parallel Simulator (LAMMPS)[41] with its ReaxFF module,[42] which describes all the interactions among Al and O atoms.[43] Cubic simulation cells were used for nanoclusters at 1, 12, and 160 atm of O_2 pressure for which the corresponding side lengths were 298, 138, and 65 Å. As the oxidation reaction proceeds, the simulation box shrinks in order to keep the pressure constant. We carefully checked that the gap between a nanocluster and its periodic images was greater than 20 Å during the whole simulation in order to avoid self-interactions. Initial velocities were randomly assigned following a Maxwell-Boltzmann distribution. Periodic boundary conditions were used in three dimensions.

The nanoclusters were subject to three different O_2 pressures: 1, 12, and 160 atm in an NPT regime (constant number of atoms, pressure, and temperature) with a time-step of 0.2 fs using the Nose-Hoover algorithm. This entails that as the O_2 reacts with the metallic nanocluster the volume of the simulation cell decreases so as to keep the pressure constant. This scenario is more realistic than the NVT regime (constant number of atoms, volume, and temperature), in which the oxygen pressure decreases as the reaction proceeds.

It was found that reaction speed is proportional to oxygen pressure. Indeed, at the lowest pressure value (1 atm) the reaction is so slow that it becomes infeasible for a systematic study within our simulation approach. At intermediate oxygen pressures (12 atm) the nanocluster suffers fragmentation, which also make the structures useless for further studies. This phenomenon of oxide cluster formation with a variety of aluminum-oxygen ratios have been found before both in simulations,[44,45] and experiments.[46,47] Fragmentation was also found at 1 atm of O_2 pressure. Details concerning geometry configurations and temperature of the corresponding nanoclusters are given in the SI. Finally, at 160 atm, the oxidation is fast and without any sign of fragmentation, we therefore chose this set up for the following calculations as a means of obtaining passivated aluminium cluster structures. This value of pressure corresponds to the lowest value studied in ref.[43]

Given that the most essential part of a MD simulation is the force field used, we dedicate a few lines to explain its validation. The Al-O ReaxFF has been proven to qualitatively predict the oxidation kinetics of aluminum slabs and nanoclusters as a function of temperature.[43] In order to take the validation one step further, we performed DFT relaxations of small Al_xO_y clusters, and compared the resulting structures and energies with that obtained by the ReaxFF. This study showed that ReaxFF favors the coordination of oxygen with four Al neighbors (inside an aluminum tetrahedron), while for DFT three Al neighbors is energetically more stable (inside an aluminum triangle). Also, the force field tends to overestimate the formation energy (see eq. 2). However, the energy discrepancy diminishes as the cluster becomes larger, where quantum effects are less accentuated. Despite these deviations, ReaxFF correctly estimates the relative energy among structures (see the supporting information for details).

For the simulated annealing calculations the oxidized aluminum nanocluster were first relaxed, then the temperature was increased from 0 K to 800 K, and then decreased to 0 K in an NVT ensemble using a Nose-Hoover thermostat during 200 ps. In order to analyze the degree of oxidation of such structures, the same criteria as in ref.[43] was used. Aluminum atoms are classified according to the percentage of metallic neighbors up to a radius of 3.2 Å, they are considered as metal (more than 90%), suboxide (between 60% and 90%), oxide (between 40% and 60%), peroxide (less than 40%). Then, each aluminum atom is counted between two radial distances r, and $r+dr$ from the central atom (the atom closer to the nanocluster center of mass). To cancel out the increase of shell volume with r, this count is divided by $N(r)$, which is the shell volume (V_s) times the density of the Al fcc bulk (ρ).

$$N(r) = \frac{n}{V_s \rho} \tag{1}$$

For comparison of stabilities the formation energy was calculated as

$$E_f = \frac{E(n)_{AlO} - E_{Al} - nE_{O_2}/2}{n} \tag{2}$$

View Article Online
DOI: 10.1039/C7NR04904H

where $E(n)_{AlO}$ is the energy of an oxide cluster with n number of oxygen atoms, E_{Al} the energy of a bare aluminum cluster, and E_{O_2} the energy of an oxygen molecule.

2.2 Density Functional Theory

Density Functional Theory (DFT) calculations were performed using the Quantum Espresso/PWSCF code.[48] Vanderbilt ultrasoft pseudopotentials[49] were used together with the Perdew-Burke-Ernzerhof (PBE)[50] approximation to the exchange-correlation functional. A 30 Ry kinetic energy cutoff and a 300 Ry charge density cutoff where used. Only the Gamma point was considered in the electronic structure calculations owing to the finite nature of the system. Geometry relaxations were converged when forces were less than 0.02 eV/Å. Unit cells were big enough so that clusters were separated by at least 12 Å from their periodic images. DFT calculations where used to validate the Reax Force Field. We performed DFT relaxations of small Al_xO_y clusters, and compared the resulting structures and energies with that obtained by the ReaxFF. The results of these calculations are shown in the Supporting Information

2.3 Time Dependent Density Functional Tight Binding

All spectra and plasmon lifetimes where calculated in the framework of the self-consistent-charge density-functional-tight-binding (SCC-DFTB) method.[51–53] This method is based on a controlled approximation of density functional theory (DFT) and has been successfully employed to describe the electronic structure and quantum properties of large organic and bio-inorganic systems.[53,54] The DFTB Hamiltonian is based on a second order expansion of the the full Kohn-Sham energy in the neighborhood of a reference density consisting of the superposition of atomic densities up to second order. The exact second order expansion is then approximated as the sum of a band energy term, a self-consistent energy term consisting of the damped electrostatic interaction between Mulliken charges and a local Hubbard like term plus an empirical repulsive term. All three body center integrals in the energy functional expression are neglected and compensated by the empirical repulsion. All two body Hamiltonian and Overlap matrix elements are explicitly calculated using a pseudopotential to represent core electrons and a minimal valence basis consisting of slater type orbitals. For all time-dependent calculations, since the nuclei are frozen, only the exactly calculated terms appear and the sole approximations are the self-consistent Hamiltonian component as well as the neglect of three center integrals[51].

The electronic structure of the ground state (GS) in all studied systems, was calculated using the DFTB+ package,[55] which is an implementation of the SCC-DFTB method. The DFTB+ code is used to compute the GS Hamiltonian (H_{GS}) and overlap ma-trix (S) and thus to obtain the initial GS reduced single-electron density matrix (ρ).The matsci-0-3[56,57] DFTB parameter set was employed in order to obtain the electronic structure for both bare aluminum and aluminum oxide nanoclusters. This parameter set includes d orbitals for aluminum atoms, extending the minimal basis set normally used in DFTB.

The methodology applied to describe electronic dynamics of the whole system is based on the real-time propagation of the reduced single-electron density matrix (ρ) under the influence of an time-varying external potential. This approximation is an extension of SCC-DFTB model to the time domain and allow us to obtain valuable information about electronic dynamics triggered by an external perturbation. The simulations all proceed through the numerical integration of the single electron density matrix equation of motion (EOM) within the the SCC-DFTB model. This equation of motion is non-linear, since the Hamiltonian depends on the density matrix via the self-consistent terms and includes the same physics, albeit approximately, as the full fledged TD-DFT framework using a time local exchange correlation functional with the advantage that it can be applied to much larger systems using relatively modest computational resources. Our implementation uses General Purpose Graphical Computing Processors (GP-GPUs) in order to accelerate the computational integration of the EOM. The method has been described in detail in[58,59].

The results shown correspond to two types different types of external time-varying potential. For the calculation of absorption spectra, the external potential corresponds to a Dirac Delta potential applied a $t = 0^-$. For this calculations we use a scheme equivalent to that originally proposed by Yabana and Bertsh[60]. After application of the perturbation the evolution of the density matrix is used to obtain the time dependent dipole moment. The Dirac Delta potential intensity ensures that the system evolves within the linear response regime. The conditions for this are described in Yabana and Bertsh's work[60]. Absorption spectra are obtained after a Fourier transform of the dipole signal and deconvolution, which in the case of a Dirac Delta perturbation amounts to a mere multiplication. In order to adequately deal with the finite time over which the EOM is evolved, the time dependent dipole moment signal is exponentially damped using a time constant of 10 fs. This amounts to adding a homogeneous broadening to all spectral lines of 0.033 eV.

Plasmon lifetimes can in principle be obtained directly from the spectra, as has been shown in the literature[61,62], by fitting the plasmon peak to a Lorentzian lineshape. We have found, however, that from a time dependent perspective it is more convenient and reproducible to calculate the lifetime directly from the dipolar signal damping in response to a monochromatic continuous perturbation. The intensity of this perturbing signal being equivalent to the one one described in the previous paragraph to ensure that the system evolves within the linear response regime. We have used this method in order to describe the Chemical Interface Damping caused by molecular adsorption on silver clusters[63]. Working within the linear response framework, our method describes the plasmon lifetime arising from pure dephasing of excitations close in energy to the plasmon peak. This method is useful for large particles in which a saturation of the dipole signal is observed, i.e. a quasi stationary state is reached.

3 Results and discussion

This section is divided in three parts: first, t he o ptical properties of different bare icosahedral aluminum nanoclusters are analyzed; then, the molecular dynamics procedure used to build

View Article Online
DOI: 10.1039/C7NR04904H

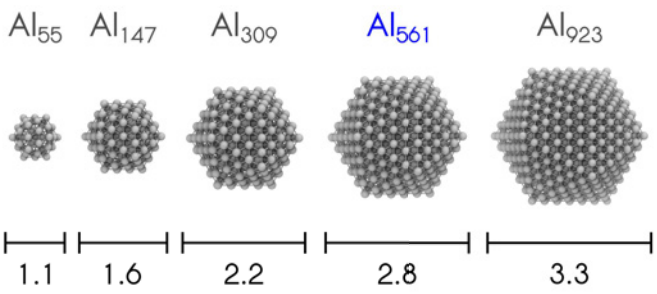

Fig. 1 Schematic representation of different bare icosahedral aluminum nanostructures that have been considered within the present report. The number of aluminum atoms and the diameter in nanometers of all particles are indicated in the scheme.

oxidized structures from the bare aluminum nanostructures is shown; and finally, the influence of oxygen on the optical absorption properties are revealed.

3.1 Bare icosahedral Aluminum Nanoclusters

Gold, silver, and aluminum present a face centered cubic (fcc) crystalline lattice, their lattice constant being 4.08 Å, 4.09 Å, and 4.05 Å, respectively. Several structures were studied for all the nanocluster sizes considered in this study, in each case we found that the icosahedral structure is the most stable. Details regarding geometries and energetics are given in the SI.. In this report, different bare icosahedral aluminum nanoclusters, ranging from 1.1 nm to 3.3 nm, were considered. A schematic representation of the aluminum nanostructures studied are shown in Figure 1.

Aluminum belongs to the boron group, its valence electrons occupy only s- and p- orbital shells. However, in our calculation, the d- electron orbital shell was also included in order to achieve a suitable description of aluminum optical and structural properties. Figure 2a shows the optical absorption spectra corresponding to the aluminum nanostructures shown in Figure 1. All the spectra are characterized by the presence of a single dipole surface plasmon resonance (SPR) band located near on $\sim$ 5 eV ($\sim$ 248 nm) in the ultraviolet region in agreement with previous reports[9–11,13].The fact that a single dipolar SPR band is observed is to be expected given the size of the particles, precluding multipolar bands to show any appreciable cross section, and in accordance to their symmetric shape that does not allow a geometric splitting of the band as would be the case for rod like particles, for example. An increase in intensity of dipole SPR band is simultaneously detected with a small redshift of plasmonic excitation energy when the particle size increases in agreement with other experimental[11] and theoretical[9–11] reports.

The plasmonic properties of bare aluminum nanoclusters resemble that of silver nanoclusters[9]. The optical absorption spectra of both metals are characterized by a single dipole SPR band without a detectable contribution of interband electronic transitions to the optical absorption spectrum. However, in the aluminum case, the redshift is less pronounced and less sensitive to particle size than in the case of silver. The density of states (DOS) and projected density of states (pDOS) over electron orbital shells of a bare icosahedral nanocluster (Al_{561}) are shown in Figure 2b. It is important to stress that the sp-band spreads through the whole electronic energy window, from occupied to unoccupied states. On the other hand, the d-band is mainly composed by unoccupied states (above the Fermi energy).

In order to explore the underlying electron dynamics triggered by the light absorption process, a bare icosahedral Al_{561} nanocluster is illuminated with a frequency in tune with the excitation energy of the SPR band as is outlined in the Figure 2d. The excited electron dynamics at the frequency of plasmonic excitation (Figure 2a, blue solid line, 5.03 eV or 246 nm) is shown in the Figure 2c. The electron dynamics is characterized by the depopulation of molecular states below Fermi energy, states associated to the sp-band (green and blue lines), and the population of unoccupied molecular states mainly associated with the d-band (red line). This dynamical picture captures all the electronic transitions that are related with plasmonic excitation. In this sense, the optical response of aluminum resembles that of silver since both show collective intraband transitions. The time dependent populations for a range of energies are shown in Figure 2d. These are obtained from projecting the instantaneous density matrix onto the ground state orbitals. The populations show oscillations in tune with the plasmon frequency for a range of energies, in agreement with results by Townsend *et al*[64].

The time dependent dipole moment ($\mu_x(t)$) obtained from an illumination simulation is a direct emergent of the electron dynamics and can be used to determine both the homogeneous line width (Γ) and the related lifetime (T_2) associated with the plasmonic excitation. This approach have been recently employed by us to determine the homogeneous line width associated with dipole SPR band for different capped and naked silver nanoclusters.[63] Here, the same model that relate the time-dependent dipole moment with homogeneous line width has been adopted obtaining the following equation

$$\Lambda(t,\Gamma) = k_1\{exp(\frac{-\Gamma t}{2}) - 1\} + k_2\{exp(\frac{-\Gamma t}{2}) + 1\} \qquad (3)$$

here k_1 and k_2 are constant independent of Γ and are related to the absorption coefficient and electric field strength. The obtained dipole moment for aluminum and silver nanoclusters with 561 atoms and its respective fitting are shown in Figure 3. The homogeneous line width and lifetime associated with plasmonic excitation for both metals are summarized in the Table 1. As it can be seen, marked differences exist between both dipole moment profiles. The homogeneous line width associated with the Al_{561} nanocluster ($\Gamma_{Al_{561}}$) is larger than the corresponding to Ag_{561} nanocluster ($\Gamma_{Ag_{561}}$). This difference means that the natural mechanisms of plasmon dephasing are increased in the aluminum case. Likewise, the spectroscopic feature associated with dipole SPR band can be characterized by other important parameter, the quality factor(Q). In this case, Q_{Ag} is larger than Q_{Al} in agreement with other theoretical reports.[9]

View Article Online
DOI: 10.1039/C7NR04904H

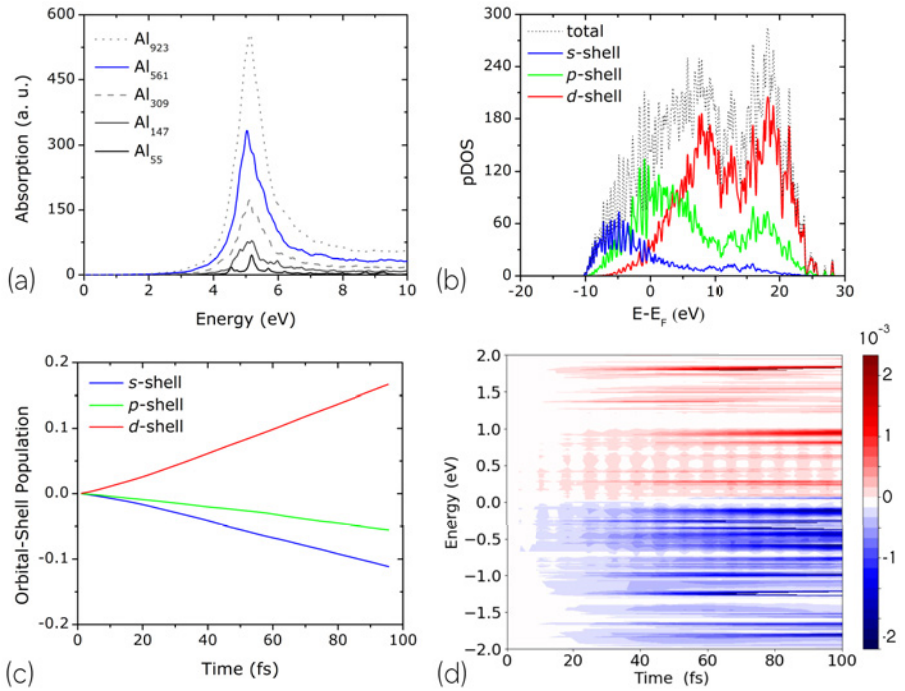

Fig. 2 **a**) Optical absorption spectra corresponding to bare icosahedral aluminum nanostructures shown in the Figure 1. **b**) Total (black dot) and projected density of states over aluminum electron orbital shells (s-shell, p-shell and d-shell) for a bare icosahedral Al_{561} nanocluster, the absoprtion spectrum of which is highlighted in blue color in **a**). **c**) Electron orbital population dynamics resulting from continuous light irradiation at dipole SPR band (5.03 eV) for a bare icosahedral Al_{561} nanocluster. **d**) Time dependent population of ground states orbitals as a function of their energy as time proceeds. Oscillations in tune with the plasmon can be seen for a range of energies.

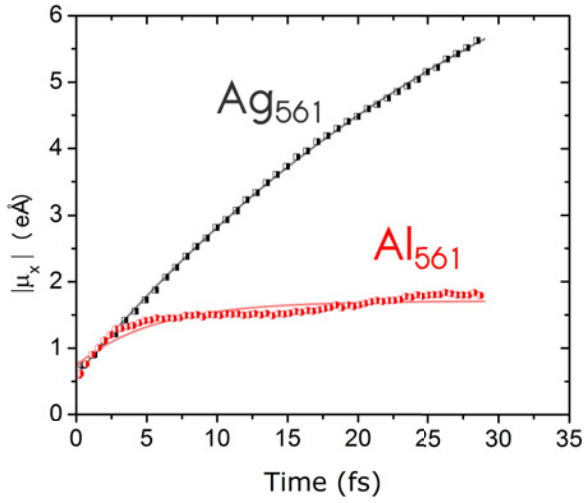

Fig. 3 Absolute value of the extrema of the dipole moment signal on the x-direction and its respective fitting curve for both siver (black line) and aluminum (red line) nanoclusters illuminated in resonance with their respective plasmon frequencies.

Table 1 The homogeneous line width, lifetime, SPR energy and quality factor for silver and aluminum nanoclusters

Nanocluster	Line width (meV)	Lifetime (fs)	E_{SPR} (eV)	Quality factor
Ag_{561}	57.0	23.1	2.90	50.91
Al_{561}	354.5	3.7	5.03	13.82

3.2 Aluminum Oxide Nanoclusters

Molecular dynamics simulations were performed for several aluminum nanoclusters at 300 K and 160 atm of oxygen pressure in an NPT ensemble. The evolution of the reaction was followed by plotting both the percentage of dissociated O_2 and the percentage of pure Al atoms during the simulation, as shown in Fig. 4a. The equilibrium of the oxidation process at this pressure is reached in the order of 40 ps. At this point there is still ∼70% of O_2 in the gas phase and ∼8% of metallic Al in the cluster. These are indications of a passivation effect in which the oxide formed prevents the oxidation from continuing. As explained above, the high pressure at which the aluminum nanoclusters is under was chosen in order to accelerate the reaction. However, this may entail that the oxidized cluster is trapped in a configuration far from that of minimum energy. It is reasonable to expect that at lower oxygen pressure (and therefore lower oxidation rate) the NP would have longer time to explore the potential energy surface and find lower energy configurations. In order to circumvent this problem, simulated annealing was performed on three stages of oxidation: A, B, and C, shown in Fig. 4a. This procedure allows the struc-

View Article Online
DOI: 10.1039/C7NR04904H

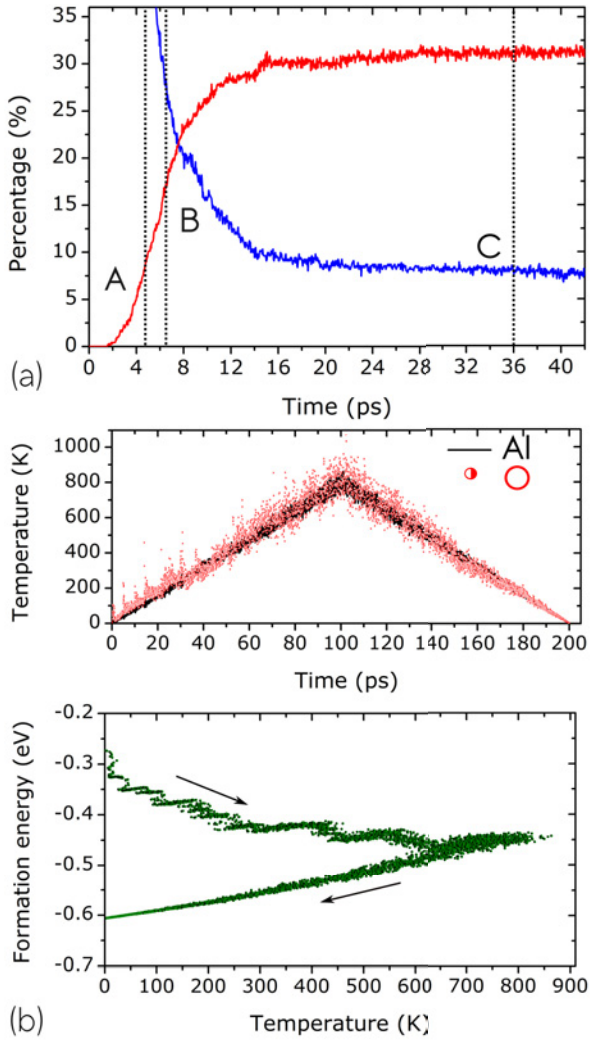

Fig. 4 (a) Percentage of reacted O_2 (over the total O_2), and of pure Al atoms (over the total Al atoms) during a simulation of Al_{561} in a NPT ensemble at 300 K under 160 atm. Three stages were selected for further studies: at 25% of the equilibrium oxidation (A), at 50% (B), and at 100% (C). **(b)** Standard annealing procedure performed on Al_{561} on the three previous stages shown. The annealing of structure A is shown as an example. Top: Temperature of Al and O atoms during the simulation. Bottom: Formation energy as a function of temperature. The arrows show the order of appearance of the points during the simulation.

tures A, B, and C to find considerably more stable configurations without changing the oxidation degree. As an example, the simulated annealing of stage A is shown in Fig 4b. Since oxygen atoms are much lighter than aluminum atoms, their temperature fluctuates more. After annealing, the oxidized aluminum nanocluster is 0.3 eV per oxygen atom more stable than the initial state, manifesting the intrinsic instability of the oxidized nanocluster generated during the original simulation.

The structures of the oxidized nanoclusters after annealing are given in Fig. 5a. Their degree of oxidation were studied through the species populations shown in Fig. 5b. Despite the increase in the number of sub-oxidized species, their degree of penetration remains almost constant (up to 5 Å from the nanocluster central atom). The oxide species are virtually absent in stages A and B, while on stage C they become significant and appear at distances from the central atom at which the metallic species disappear.

3.3 Electronic vs geometric effect

The optical absorption spectra of structures A, B, and C are shown in Fig. 5c. An increase in thickness of the oxide layer produces an optical response that is characterized by red-shift, a broadening and decrease in the intensity of dipole SPR band associated with aluminum nanostructures. This optical behavior is in good agreement with other theoretical and experimental reports.[10–12]. Halas *et al* report how an oxide layer lowers the energy and intensity of the dipolar plasmon resonance in Al nanodisks[11]. The same effect is reported from theoretical calculations based on the discrete dipole approximation by Zeng *et al*. Reports in the literature are for very large structures[10–12] and therefore well described by classical models. Our results, despite showing the same qualitative features, show that these carry on down to very small sizes and resemble the main spectroscopic changes that characterize chemical interface damping[63]. Our calculations extend the results present in the literature to a regime where the atomic structure comes into play and allow a deeper insight into the chemical effects on the plasmon lifetime and their relation to disorder.

The most intuitive interpretation of these results is that oxygen is directly affecting the plasmonic properties of aluminum. However, one could argue that it is the breakage of the highly symmetric structure what weakens the plasmonic signal, in which case the oxide would be affecting the plasmon indirectly. In order to determine which effect is dominant, a totally random structure of bare Al_{561} was created. A comparison of the electronic properties of the latter with that of a perfect icosahedral Al_{561} should manifest the geometric effect. Icosahedral and random Al_{561} were thermalized at 300 K during 200 ps. The latter was created by taking away the oxygen atoms of structure C and then thermalizing. Fig 6a shows the resulting structures. It can be seen that the icosahedral structure retains its geometry during the simulation. The radial distribution function $g(r)$ of the metallic nanoclusters is given in Fig 6b. As expected, peaks of the random structure are wider and lower with respect to those of the icosahedral structure, indicating a larger deviation from the atomic crystal positions. Moreover, the peak of second neighbors found in the icosahedral structure is missing in the random structure.

As shown by the optical absorption spectrum of icosahedral and random Al_{561} in Fig. 6c, the loss of symmetry only produces mild modifications o ver t he o ptical r esponse. T his r esult determines that the weakening of the plasmonic signal on AlO nanoclusters can only be attributed to the electronic effect induced by oxidation. A deeper insight over the effect of oxide formation can be obtained analyzing the projected density of state and electron dynamics, Fig 7. As it can been seen in the a), c) and c) panels of Fig. 7, the increase in thickness of the aluminum oxide layer gradually produces a separation of the continuous and featureless metallic density of states of the bare cluster (shown in Fig. 2b) into what constitutes the seeds of the conduction (lower energy) and valence (higher energy) bands of the pure oxide. A gap of reduced density of states around 5 eV below the Fermi level can be

View Article Online
DOI: 10.1039/C7NR04904H

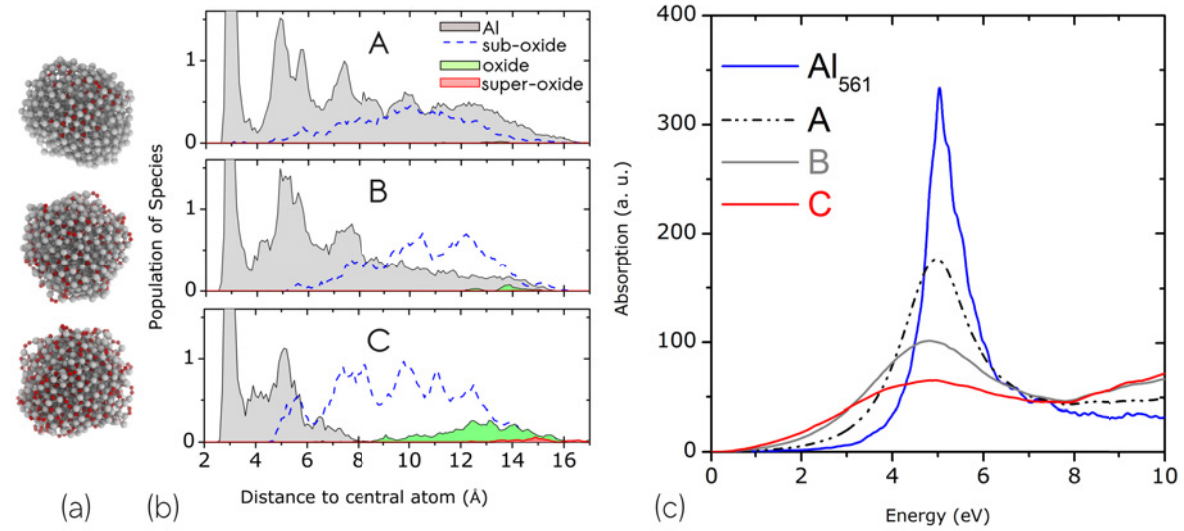

Fig. 5 **(a)** Configuration of AlO corresponding to structures A, B, and C after the annealing procedure. **(b)** Species distribution around the nanocluster central atom for structures A, B, and C. **(c)** Optical absorption spectra of the icosahedral Al_{561} nanocluster and the corresponding oxidized structures A, B, and C.

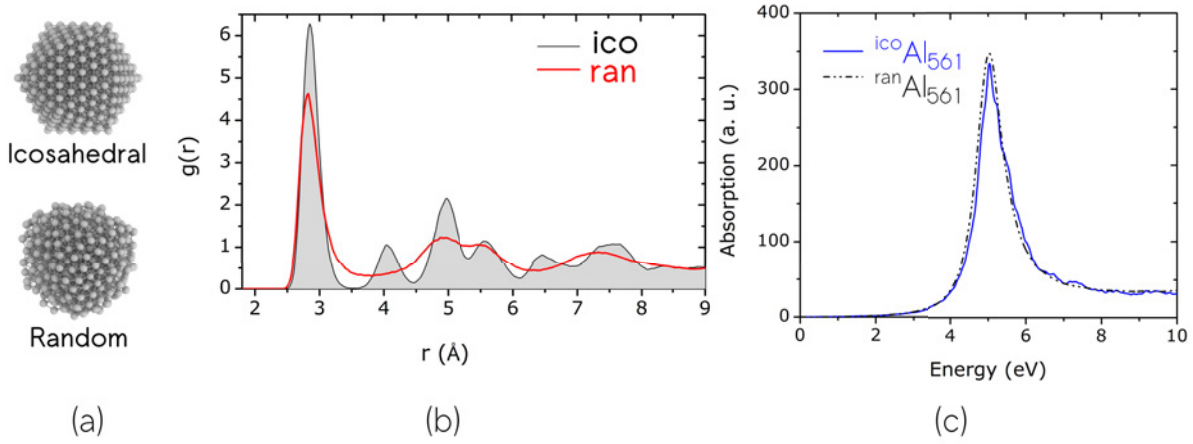

Fig. 6 **(a)** Schematic view of an icosahedral (ico) and a random (ran) Al_{561} nanocluster. **(b)** Radial distribution function of both nanoclusters. **(c)** Optical absorption spectrum of (black solid line) perfect icosahedral and (red solid line) bare Al_{561} nanoclusters.

clearly seen to deepen upon increasing oxidation. The lower energy (valence) band is mainly composed by oxygen orbitals while the lower energy (conduction) band is mainly composed by aluminum orbitals. There is a significant c hange a t t he d ensity of states at the Fermi level. Whereas in the bare metallic cluster the DOS is monotonically increasing at the Fermi level, a peak is formed upon oxidation, that sharpens with increasing oxidation. Both the formation of a pseudo-gap below the Fermi level and the changes in the DOS at the Fermi level point to a a diminishing of the metallic character of the particle. This weakening of metallic character induces more attenuated electron dynamics as can be seen in the panel e), f) and g) inside of Fig.7.

4 Conclusion

We have presented results of molecular dynamics simulations with a reactive force field combined with time-dependent density functional tight binding (TD-DFTB) simulations to describe the oxidation process of bare icosahedral aluminum nanoclusters and to explore the modifications that this oxidation causes on their optical absorption properties. It was found that oxygen induces a redshift and a broadening of the dipole surface plasmon resonance (SPR) band, which is in good agreement with both theoretical and experimental reports. These effects are only attributed to oxidation and not to the loss of the crystalline structure caused by the oxidative process. To the best of our knowledge, this is the first report that addresses the issue of the modification of optical properties of sizable metallic clusters due to oxidation through the combination of a series of atomistic methods that go from classical to quantum dynamics taking fully into account the atomic structure of the system.

View Article Online
DOI: 10.1039/C7NR04904H

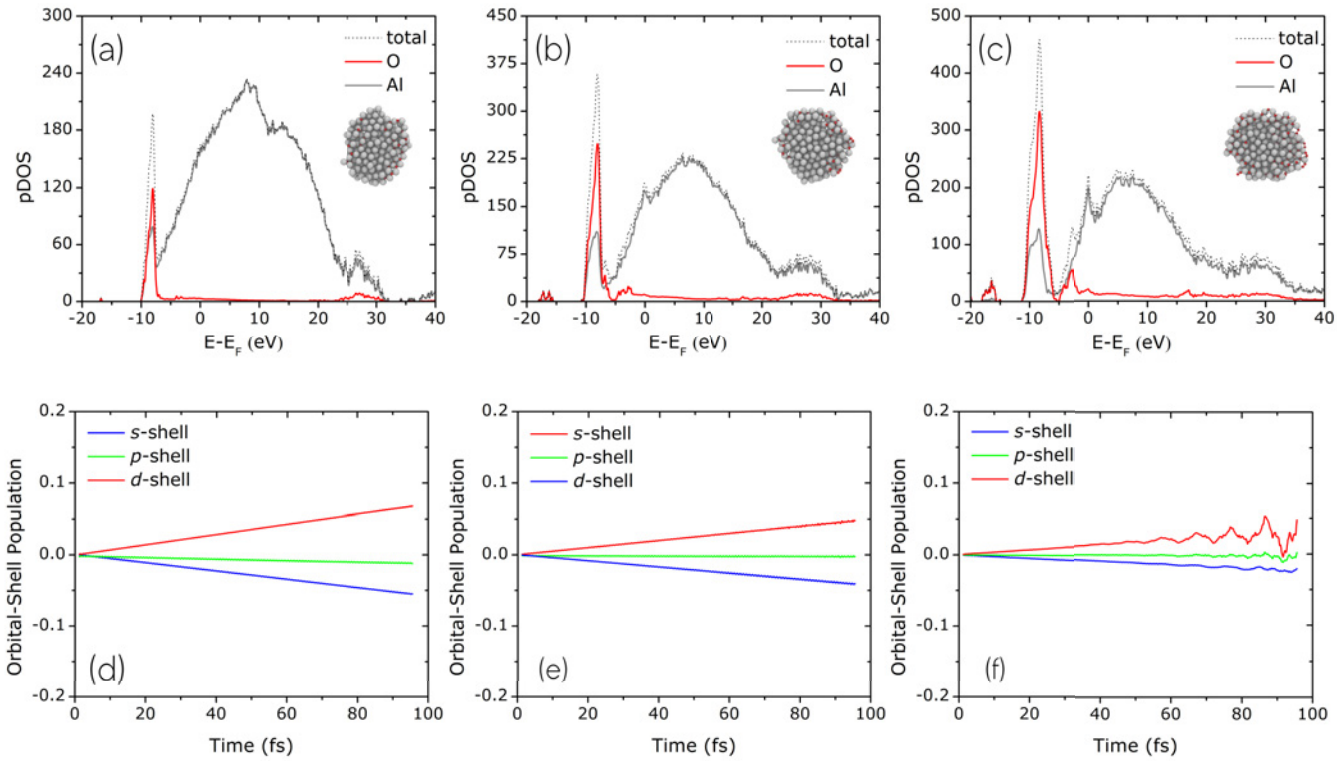

Fig. 7 a),b) and **c)**: Total density of states (black dot) and projected density of state over aluminum (gray solid line) and oxygen (red solid line) electron orbital shells for the corresponding oxidized structures A, B, and C. **d),e)** and **f)**: Electron orbital population dynamics resulting from continuous light irradiation at dipole SPR band for the corresponding oxidized structures A, B, and C.

5 Acknowledgements

The authors acknowledge financial support by Consejo Nacional de Investigaciones Científicas y Técnicas (CONICET) through Grant PIP 112-201101-0092 and PIP 11220110100992, FONCyT PICT-2015-2191, and SeCyT-UNC. This work has used computational resources from CCAD, Universidad Nacional de Córdoba (http://ccad.unc.edu.ar/), in particular the Mendieta Cluster, which is part of SNCAD-MinCyT, República Argentina. O.A.D.-G. thanks CONICET for a postdoctoral fellowship.

References

1 S. Link and M. A. El-Sayed, *International Reviews in Physical Chemistry*, 2000, **19**, 409–453.
2 S. Link and M. A. El-Sayed, *Annual Review of Physical Chemistry*, 2003, **54**, 331–366.
3 G. V. Hartland, *Chemical Reviews*, 2011, **111**, 3858–3887.
4 N. G. Khlebtsov and L. A. Dykman, *Journal of Quantitative Spectroscopy and Radiative Transfer*, 2010, **111**, 1 – 35.
5 E. A. Coronado, E. R. Encina and F. D. Stefani, *Nanoscale*, 2011, **3**, 4042–4059.
6 D. Jaque, L. Martinez Maestro, B. del Rosal, P. Haro-Gonzalez, A. Benayas, J. L. Plaza, E. Martin Rodriguez and J. Garcia Sole, *Nanoscale*, 2014, **6**, 9494–9530.
7 A. Comin and L. Manna, *Chem. Soc. Rev.*, 2014, **43**, 3957–3975.
8 G. V. Naik, V. M. Shalaev and A. Boltasseva, *Advanced Materials*, 2013, **25**, 3264–3294.
9 M. B. Ross and G. C. Schatz, *Journal of Physics D: Applied Physics*, 2015, **48**, 184004.
10 J. Hu, L. Chen, Z. Lian, M. Cao, H. Li, W. Sun, N. Tong and H. Zeng, *The Journal of Physical Chemistry C*, 2012, **116**, 15584–15590.
11 M. W. Knight, N. S. King, L. Liu, H. O. Everitt, P. Nordlander and N. J. Halas, *ACS Nano*, 2014, **8**, 834–840.
12 D. Gérard and S. K. Gray, *Journal of Physics D: Applied Physics*, 2015, **48**, 184001.
13 S. Mandal, J. Wang, R. E. Winans, L. Jensen and A. Sen, *The Journal of Physical Chemistry C*, 2013, **117**, 6741–6746.
14 J. Martin and J. Plain, *Journal of Physics D: Applied Physics*, 2015, **48**, 184002.
15 K. L. Kelly, E. Coronado, L. L. Zhao and G. C. Schatz, *The Journal of Physical Chemistry B*, 2003, **107**, 668–677.
16 E. Hao, S. Li, R. C. Bailey, S. Zou, G. C. Schatz and J. T. Hupp, *The Journal of Physical Chemistry B*, 2004, **108**, 1224–1229.
17 A. Brioude, X. C. Jiang and M. P. Pileni, *The Journal of Physical Chemistry B*, 2005, **109**, 13138–13142.
18 H. E. Johnson and C. M. Aikens, *The Journal of Physical Chemistry A*, 2009, **113**, 4445–4450.
19 G.-T. Bae and C. M. Aikens, *The Journal of Physical Chemistry C*, 2012, **116**, 10356–10367.
20 C. M. Aikens, S. Li and G. C. Schatz, *The Journal of Physical Chemistry C*, 2008, **112**, 11272–11279.

View Article Online
DOI: 10.1039/C7NR04904H

21 O. Baseggio, M. De Vetta, G. Fronzoni, M. Stener, L. Sementa, A. Fortunelli and A. Calzolari, *The Journal of Physical Chemistry C*, 2016, **120**, 12773–12782.

22 M.-S. Liao, P. Bonifassi, J. Leszczynski, P. C. Ray, M.-J. Huang and J. D. Watts, *The Journal of Physical Chemistry A*, 2010, **114**, 12701–12708.

23 R. L. Gieseking, M. A. Ratner and G. C. Schatz, *The Journal of Physical Chemistry A*, 2016, **120**, 9324–9329.

24 M. Kuisma, A. Sakko, T. P. Rossi, A. H. Larsen, J. Enkovaara, L. Lehtovaara and T. T. Rantala, *Phys. Rev. B*, 2015, **91**, 115431.

25 F. Rabilloud, *The Journal of Chemical Physics*, 2014, **141**, 144302.

26 B. Bousquet, M. Cherif, K. Huang and F. Rabilloud, *The Journal of Physical Chemistry C*, 2015, **119**, 4268–4277.

27 G.-T. Bae and C. M. Aikens, *The Journal of Physical Chemistry C*, 2015, **119**, 23127–23137.

28 C. M. Aikens, *The Journal of Physical Chemistry A*, 2009, **113**, 10811–10817.

29 L. Sementa, G. Barcaro, O. Baseggio, M. De Vetta, A. Dass, E. Aprà, M. Stener and A. Fortunelli, *The Journal of Physical Chemistry C*, 2017, **121**, 10832–10842.

30 N. Durante, A. Fortunelli, M. Broyer and M. Stener, *The Journal of Physical Chemistry C*, 2011, **115**, 6277–6282.

31 S. Malola, L. Lehtovaara, J. Enkovaara and H. Häkkinen, *ACS Nano*, 2013, **7**, 10263–10270.

32 S. Malola, L. Lehtovaara and H. Häkkinen, *The Journal of Physical Chemistry C*, 2014, **118**, 20002–20008.

33 K. Iida, M. Noda, K. Ishimura and K. Nobusada, *The Journal of Physical Chemistry A*, 2014, **118**, 11317–11322.

34 R. W. Burgess and V. J. Keast, *The Journal of Physical Chemistry C*, 2014, **118**, 3194–3201.

35 J. Lindgren, A. Clayborne and L. Lehtovaara, *The Journal of Physical Chemistry C*, 2015, **119**, 19539–19547.

36 D. Casanova, J. M. Matxain and J. M. Ugalde, *The Journal of Physical Chemistry C*, 2016, **120**, 12742–12750.

37 R. Sinha-Roy, X. López-Lozano, R. L. Whetten, P. García-González and H.-C. Weissker, *The Journal of Physical Chemistry C*, 2017, **121**, 5753–5760.

38 H.-C. Weissker and C. Mottet, *Phys. Rev. B*, 2011, **84**, 165443.

39 G. Barcaro, M. Broyer, N. Durante, A. Fortunelli and M. Stener, *The Journal of Physical Chemistry C*, 2011, **115**, 24085–24091.

40 S. Malola, M. J. Hartmann and H. Häkkinen, *The Journal of Physical Chemistry Letters*, 2015, **6**, 515–520.

41 S. Plimpton, *Journal of Computational Physics*, 1995, **117**, 1–19.

42 H. Aktulga, J. Fogarty, S. Pandit and A. Grama, *Parallel Computing*, 2012, **38**, 245–259.

43 S. Hong and A. C. van Duin, *J. Phys. Chem C*, 2015, **119**, 17876–17886.

44 T. J. Campbell, G. Aral, S. Ogata, R. K. Kalia, A. Nakano and P. Vashishta, *Phys. Rev. B*, 2005, **71**, 205413.

45 Y. Li, R. K. Kalia, A. Nakano and P. Vashishta, *Journal of Applied Physics*, 2013, **114**, 134312.

46 T. N. Piehler, F. C. DeLucia, C. A. Munson, B. E. Homan, A. W. Miziolek and K. L. McNesby, *Appl. Opt.*, 2005, **44**, 3654–3660.

47 S. Wang, Y. Yang, Z. Sun and D. D. Dlott, *Chemical Physics Letters*, 2003, **368**, 189–194.

48 P. Giannozzi, S. Baroni, N. Bonini, M. Calandra, R. Car, C. Cavazzoni, D. Ceresoli, G. L. Chiarotti, M. Cococcioni, I. Dabo, A. Dal Corso, S. de Gironcoli, S. Fabris, G. Fratesi, R. Gebauer, U. Gerstmann, C. Gougoussis, A. Kokalj, M. Lazzeri, L. Martin-Samos, N. Marzari, F. Mauri, R. Mazzarello, S. Paolini, A. Pasquarello, L. Paulatto, C. Sbraccia, S. Scandolo, G. Sclauzero, A. P. Seitsonen, A. Smogunov, P. Umari and R. M. Wentzcovitch, *Journal of Physics: Condensed Matter*, 2009, **21**, 395502 (19pp).

49 D. Vanderbilt, *Phys. Rev. B*, 1990, **41**, 7892–7895.

50 J. P. Perdew, K. Burke and M. Ernzerhof, *Phys. Rev. Lett.*, 1996, **77**, 3865–3868.

51 M. Elstner, D. Porezag, G. Jungnickel, J. Elsner, M. Haugk, T. Frauenheim, S. Suhai and G. Seifert, *Phys. Rev. B*, 1998, **58**, 7260–7268.

52 M. Elstner and G. Seifert, *Philosophical Transactions of the Royal Society of London A: Mathematical, Physical and Engineering Sciences*, 2014, **372**, 20120483.

53 A. S. Christensen, T. Kubař, Q. Cui and M. Elstner, *Chemical Reviews*, 2016, **116**, 5301–5337.

54 M. Gaus, Q. Cui and M. Elstner, *Wiley Interdisciplinary Reviews: Computational Molecular Science*, 2014, **4**, 49–61.

55 B. Aradi, B. Hourahine and T. Frauenheim, *The Journal of Physical Chemistry A*, 2007, **111**, 5678–5684.

56 J. Frenzel, A. F. Oliveira, H. A. Duarte, T. Heine and G. Seifert, *Zeitschrift für anorganische und allgemeine Chemie*, 2005, **631**, 1267–1271.

57 H. Manzano, A. N. Enyashin, J. S. Dolado, A. Ayuela, J. Frenzel and G. Seifert, *Advanced Materials*, 2012, **24**, 3239–3245.

58 M. B. Oviedo, C. F. A. Negre and C. G. Sanchez, *Phys. Chem. Chem. Phys.*, 2010, **12**, 6706–6711.

59 C. F. A. Negre, V. C. Fuertes, M. B. Oviedo, F. Y. Oliva and C. G. Sánchez, *The Journal of Physical Chemistry C*, 2012, **116**, 14748–14753.

60 K. Yabana and G. F. Bertsch, *Physical Review B*, 1996, **54**, 4484–4487.

61 C. Negre and C. G. Sánchez, *The Journal of chemical physics*, 2008, **129**, 034710.

62 J. Lermé, *The Journal of Physical Chemistry C*, 2011, **115**, 14098–14110.

63 O. A. Douglas-Gallardo, M. Berdakin and C. G. Sánchez, *The Journal of Physical Chemistry C*, 2016, **120**, 24389–24399.

64 E. Townsend and G. W. Bryant, *Nano Letters*, 2012, **12**, 429–434.